Journal of Power Sources 192 (2009) 515–524

Contents lists available at ScienceDirect

Journal of Power Sources

journal homepage: www.elsevier.com/locate/jpowsour

Thermal stress analysis of planar solid oxide fuel cell stacks: Effects of sealing design

Chih-Kuang Lin[a,*], Ling-Hao Huang[a], Lieh-Kwang Chiang[b], Yau-Pin Chyou[b]

[a] Department of Mechanical Engineering, National Central University, Jhong-Li 32001, Taiwan
[b] Nuclear Fuel & Material Division, Institute of Nuclear Energy Research, Lung-Tan 32546, Taiwan

ARTICLE INFO

Article history:
Received 17 January 2009
Received in revised form 3 March 2009
Accepted 3 March 2009
Available online 14 March 2009

Keywords:
Planar solid oxide fuel cell
Thermal stress
Multi-cell stack
Finite element analysis
Mica-based seal
Sealing design

ABSTRACT

A three-dimensional multi-cell model based on a prototypical, planar solid oxide fuel cell (pSOFC) stack design using compliant mica-based seal gaskets was constructed in this study to perform comprehensive thermal stress analyses by using a commercial finite element analysis (FEA) code. Effects of the applied assembly load on the thermal stress distribution in the given integrated pSOFC stack with such a compressive sealing design were characterized. A comparison was made with a previous study for a similar comprehensive multi-cell pSOFC stack model but using only a rigid type of glass–ceramic sealant instead. Simulation results indicate that stress distributions in the components such as positive electrode-electrolyte-negative electrode (PEN) plate, PEN-supporting window frame, nickel mesh, and interconnect were mainly governed by the thermal expansion mismatch rather than by the applied compressive load. An applied compressive load of 0.6 MPa could eliminate the bending deformation in the PEN-frame assembly plate leading to a well joined structure. For a greater applied load, the critical stresses in the glass–ceramic and mica sealants were increased to a potential failure level. In this regard, a 0.6 MPa compressive load was considered an optimal assembly load. Changing the seal between the connecting metallic PEN-supporting frame and interconnect from a rigid type of glass–ceramic sealant to a compressive type of mica gasket would significantly influence the thermal stress distribution in the PEN plate. The critical stress in the PEN was favorably decreased at room temperature but considerably increased at operating temperature due to such a change in sealing design. Such differences in the stress distribution could be ascribed to the differences in the constrained conditions at the interfaces of adjacent components under various sealing designs.

1. Introduction

Recently, solid oxide fuel cells (SOFCs) have received great attention as a promising new technology for electrical power generation. Compared with other types of fuel cells, SOFCs utilize solid ceramics as the electrolyte and electrode and operate at a higher temperature (typically 800–1000 °C). Such a high operating temperature also provides flexibility of fuel without a noble catalyst and a very high efficiency with a combination of heat and power applications. However, the fragile ceramic electrolytes and electrodes in such a high temperature would face the problem of high thermal stresses possibly leading to performance degradation. In order to enhance the durability and reliability of SOFC, to reduce its long start-up time, and to lower its fabrication cost, recent development of SOFC has been focused on reducing the operating temperature by introducing conventional metallic materials as the interconnects and frames. Planar SOFCs (pSOFCs) are being developed for use at intermediate operating temperatures (600–800 °C) due to their lower electrical resistance. In this regard, pSOFCs are classified as an intermediate-temperature SOFC (ITSOFC).

A typical unit cell in a pSOFC stack is composed of a positive electrode-electrolyte-negative electrode (PEN) assembly plate supported by a window frame, a porous nickel mesh, two end interconnects, and gas seals. In practical applications, multiple cells are usually integrated into a pSOFC stack in order to obtain a specific voltage and power output. Sealants are required at interfaces between adjacent cells as a gasket to prevent gas leakage and electrical conduction. For SOFC, the sealing approaches can be classified into rigid and compressive seals [1]. Rigid seals, primarily glasses or glass ceramics, do not require applying load during operation and have an excellent sealing efficacy. In recent years, compliant mica-based compressive seals also attract some attention. If the seals are non-bonding and compliant, individual stack components are free to expand and contract during thermal cycling [2]. Therefore, the thermal expansion mismatch of compressive seals is not as severe as that of rigid seals. Because the compressive sealant is not like the

* Corresponding author. Tel.: +886 3 426 7340; fax: +886 3 425 4501.
E-mail address: t330014@cc.ncu.edu.tw (C.-K. Lin).

0378-7753/$ – see front matter © 2009 Elsevier B.V. All rights reserved.
doi:10.1016/j.jpowsour.2009.03.010

rigid one in sealing components with tight bonding, it is replaceable, like a layered gasket, and more convenient to use. However, the use of compressive seals requires an externally applied load which could generate certain stresses in pSOFC components. In this regard, the influence of the mechanical behavior of gas seal on the thermal stress distribution in pSOFCs needs to be evaluated.

As described above, thermal stress is a major factor to affect the structural reliability of an SOFC stack due to the high operating temperature. The major sources of thermal stress in a pSOFC stack include mismatch of coefficient of thermal expansion (CTE), thermal gradient, and system configuration. Different air/fuel flow-path configurations have certain effects on the temperature distribution at operation. CTE mismatch between components in an SOFC stack is the major factor to generate thermal stresses. Because the temperature difference is very large between steady-operation and shutdown stages, even a small CTE mismatch may result in significant thermal stresses in an SOFC stack. Several issues about the stresses in SOFC stacks have been studied. A few studies [3–5] used X-ray diffraction to measure the residual stresses generated during cell fabrication. Those studies [3–5] found residual stresses might not cause failure of the PEN directly but still need to be taken into account in thermal stress analysis. A few other studies [4,6,7] were mainly focused on thermal stresses in the PEN structure caused by CTE mismatch or geometrical factors by neglecting the temperature gradients and thermal interactions between PEN and other cell components. Some other studies [8–11] conducted numerical simulations to investigate thermal stress distributions in pSOFCs by using a single-cell stack model. In particular, in those studies [8–11], for the sake of simplicity in calculation, cell components such as gas seals and the thermal interactions between cell components in a multi-cell stack were not considered. In order to provide more realistic and reliable results for practical applications, a comprehensive three-dimensional (3D) finite element analysis (FEA) model of a multi-cell stack based on a prototypical pSOFC stack design was first developed by the authors' research team to calculate the thermal stress distributions at various stages during an operation cycle [12]. In that study [12], the effects of stack support condition, viscous behavior of the glass–ceramic sealant, temperature gradient, and thermal expansion mismatch between components were systematically characterized.

As sealing design could also affect the thermal stress distribution in an SOFC stack, it is also very important to study this issue. In an earlier study [12], the thermal stresses generated at various stages of operation in a multi-cell pSOFC stack using a glass ceramic as the sealant have been systematically investigated. Weil and Koeppel [13,14] conducted thermal stress analyses for a sealing design using a metal-foil-based, bonded compliant seal (BCS) to hermetically seal the ceramic cell and adjacent metallic window frame in comparison with another two bonded sealing designs, namely glass–ceramic and air brazed seals. It was found that the glass–ceramic seal induced the highest stress concentration in the PEN and the BCS induced relatively low stresses in the PEN and sealant among the given three bonded sealing designs [14]. However, in those studies [13,14], only the thermal stress distributions in the components of ceramic cell, window frame and seal were analyzed without considering the effects of sealing design on the interactions between connecting unit cells and associated thermal stress distributions in a practical, comprehensive multi-cell pSOFC stack. In addition, uniform distributions of operating and shutdown temperatures were assumed in those studies [13,14] without considering temperature gradient effects which would occur in a practically operating pSOFC stack. As non-bonded, compliant mica-based compressive seals have recently been developed, in a way like gaskets, to seal adjacent metallic interconnects and PEN-supporting frames in multi-cell pSOFC stacks, it is important and practical to study the thermal stresses in such a compliant sealing design and make a comparison with other sealing designs. However, this important issue still lacks sufficient studies in the literature and provides a need for the current study to investigate the effects of sealing design on the thermal stress distribution in a comprehensive multi-cell pSOFC stack for practical applications.

A systematic and comprehensive analysis of thermal stress distribution is necessary for an advanced pSOFC design. To provide an effective tool for assessment of thermal stress in a pSOFC system under design stage, it would be better to use a simulation model as close as possible to the practical applications. As described above, the models used in prior work [14] to study the effect of sealing design on thermal stresses in pSOFC stack are simplified to some extent. In addition, the thermal stresses in a comprehensive multi-cell pSOFC stack using mica-based compressive seals have not yet been studied. For these reasons, a 3D multi-cell model based on a prototypical pSOFC stack design using mica-based gaskets was constructed in the current study to perform comprehensive thermal stress analyses by using a commercial FEA code. In this 3D multi-cell FEA model, the interfacial fracture between connecting components was not considered. The effects of applied compressive load on the thermal stress distribution in an integrated pSOFC stack with such a compressive sealing design was characterized. The simulation results were also made a comparison with those of a previous study [12] using a similar comprehensive multi-cell pSOFC stack model but with a bonded glass–ceramic seal instead. It is hoped that the results of the current study and previous work [12] will help predict the locations where failure may take place during various stages of SOFC operation, and help choose suitable sealants for an advanced pSOFC stack design.

2. Modeling

2.1. Finite element model

In this study, thermal stress distributions in a 3-cell pSOFC stack at various stages of operation were analyzed by using a commercial FEA code 'ABAQUS' (ABAQUS, Inc., Providence, RI, USA). The FEA model was constructed based on a stack design being developed at the Institute of Nuclear Energy Research (INER), Taiwan. Fig. 1 shows the exploded view of a half of such a 3-cell pSOFC stack. Only one half of the stack configuration is needed for building up this 3D FEA model because of its geometrical symmetry. Note that a similar 3D, 3-cell-stack FEA model was constructed and analyzed in a previous study [12] except that the mica gaskets shown in Fig. 1 were replaced by glass–ceramic sealants. Therefore, a direct comparison of the results in the current study with those in [12] would provide an insight into the effects of sealing design on thermal stress distribution in pSOFC stack. In Fig. 1, each unit cell of the 3-cell stack is composed of a PEN plate with a supporting window frame, two interconnects with gas channels, and a nickel mesh. As described above, a PEN assembly consists of anode, electrolyte, and cathode. The periphery of the PEN assembly plate was bonded to the supporting window frame by using a glass–ceramic sealant. The three unit cells were joined together to become a 3-cell SOFC stack by using a compressive mica sealant, in a way like a gasket, to seal the PEN-supporting frames and adjacent interconnects.

The dimensions of the outer edges for the top and bottom plates, interconnects, PEN-supporting frames, and mica gaskets have a length of 150 mm and a width of 100 mm. The nominal thickness of the frame and interconnect is 2 mm with gas channels in a depth of 0.8 mm. The size of the PEN is 80 mm × 80 mm × 0.7 mm. The thickness of the mica layer is 0.5 mm in order to make the PEN uniformly touch the gas channels and maintain the stack's compatibility. As the thickness of each component in the pSOFC is significantly smaller than the other dimensions, an 8-node continuum shell element (SC8R) [15] was employed in this study. From a modeling

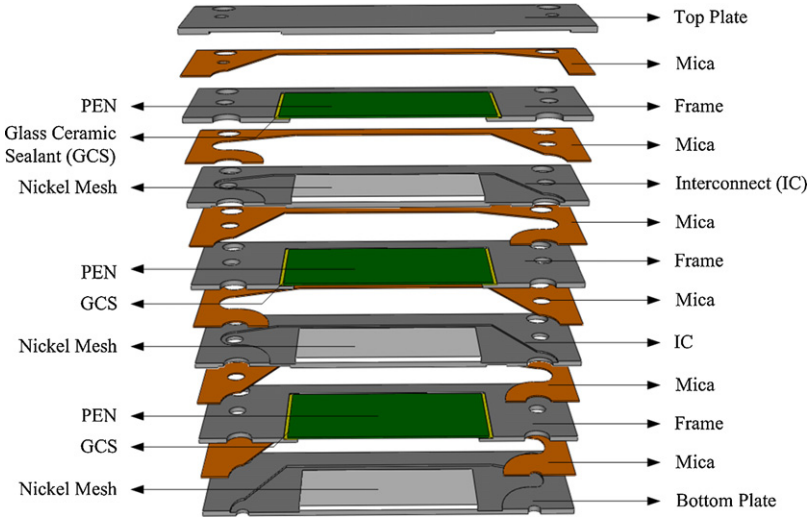

Fig. 1. Exploded view of a half of a 3-cell pSOFC stack.

point of view, continuum shell elements look like 3D continuum solids, but their kinematic and constitutive behavior is similar to that of conventional shell elements [15]. Fig. 2 shows the discrete meshes of the 3D FEA model constructed in this study. There are total 26993 elements and 47074 nodes in the 3D model shown in Fig. 2. The total number of degrees of freedom is about 187,000 in the given continuum shell elements. Note that in Figs. 1 and 2, the fuel inlet for this counter-flow pSOFC is located at the left end of the stack while the air inlet is located at the right end of the stack.

2.2. Simulation procedures

In order to evaluate the thermal stresses at each stage of an SOFC operation cycle, a multiple-step heating/cooling sequence was applied in the modeling. Unit cells are usually assembled together to form a multi-cell pSOFC stack at 800 °C to let the glass–ceramic sealant completely react and cure. Therefore, all the components in the FEA model were thus defined as stress free at 800 °C in the beginning. In the meantime, a compressive load was applied on the top plate of the pSOFC stack in order to make each layer tightly contact with each other. This compressive load is required for use of a compressive mica sealant. In earlier studies [2,16], the hermetic performance of mica-based sealants under mechanically applied compressive stresses ranging from 0.1 to 6.20 MPa was evaluated for the corresponding gas leakage rates. Accordingly, in order to investigate the effects of the applied compressive load on the thermal stress distribution in pSOFC stack, five different compressive loads (0.06, 0.1, 0.6, 1, and 6 MPa) were selected and applied in the present work. After the assembly process, the multi-cell stack model was then cooled down to room temperature (RT) for future operation. Following this step, the entire model was heated to the operating temperature. At the steady-operation stage, a set of thermal field data were imported into the FEA model. The thermal field data and temperature profile were generated by an integrated thermo-electrochemical model developed in a previous study [17]. The temperature profile at the steady-operation stage in such a 3-cell SOFC stack model has been generated in a previous study [12] and applied in the current study, as shown in Fig. 3. In this way, results of thermal stress distribution in the present work can be made a direct comparison with those in [12] under the same thermal conditions. After the steady-operation stage, the model was re-cooled down to RT, hereafter called the shutdown stage, to complete an operation cycle. Fig. 4 shows the simulation procedures for the present work. Note that in Fig. 4 the temperature is homogeneous during all steps except the steady-operation stage. In order to calculate the stresses generated by the applied compressive load only, a mechanical-load-only simulation was also conducted. In the mechanical-load-only simulation, only the applied compressive load was considered without importing the thermal field data into

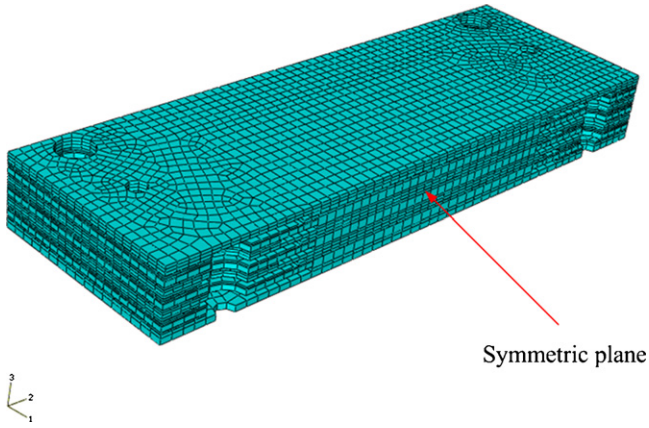

Fig. 2. Schematic of the finite element model for one half of a 3-cell pSOFC stack.

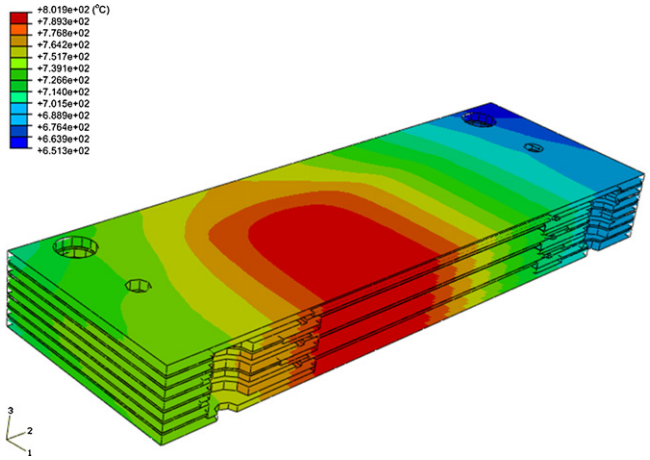

Fig. 3. Temperature distribution at the steady-operation stage in a 3-cell pSOFC stack model [12].

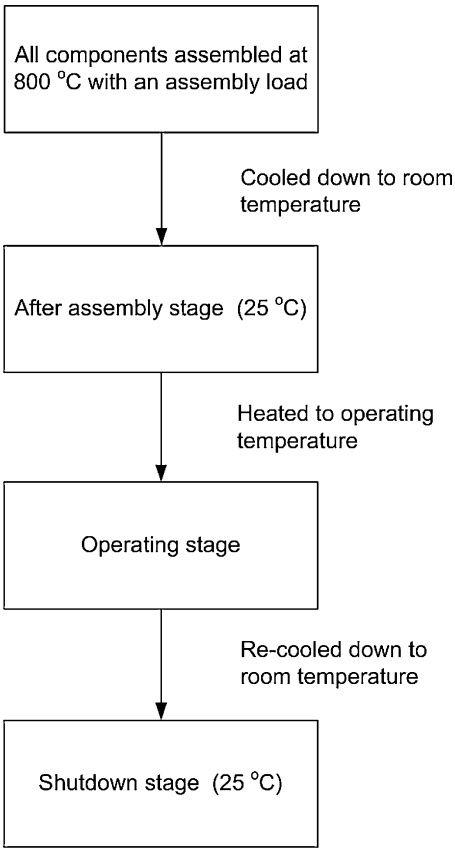

Fig. 4. Simulation procedures of thermal stress distribution.

the FEA model. By comparing the stress distributions in the models with and without thermal field data, effects of the mechanically applied load can be estimated.

2.3. Material properties and failure criteria

As shown in Fig. 1, the materials used in modeling the current pSOFC stack design include anode-supported PEN (green regions), Crofer 22-APU (PEN-supporting window frame and interconnect, gray regions), G-18 glass ceramic (rigid sealant, yellow regions), phlogopite mica (compressive sealant, orange regions), and nickel (nickel mesh, white regions). As the expected highest operating temperature for the given pSOFC stack is around 800 °C, material properties at such a high temperature and RT are needed to obtain better simulation results. All of the thermal and mechanical properties at room and high temperatures for the given materials imported into the FEA modeling can be found in [12] except the mica gasket. The elastic properties of the mica sealant are orthotropic and assumed to be equal to those of a single-crystal phlogopite mica. The elastic properties of the phlogopite mica are shown in Table 1. The value of the Young's modulus at 800 °C for the given mica was estimated based on the data at RT [18] and a temperature-dependent relationship of elastic modulus for a thin ceramic plate [19]. Thermal expansion data of a phlogopite mica [20] were used for the mica seal gasket. The Poisson's ratio of each material was assumed constant at all given stages.

Table 1
Elastic properties of phlogopite mica.

Temperature (°C)	Elastic modulus // to (0 0 1)-plane (GPa)	Elastic modulus ⊥ to (GPa)	Poisson's ratio
25	164[a]	48[a]	0.32[a]
800	122[b]	5.8[b]	0.32[a]

[a] From Ref. [18].
[b] Estimated by the RT value and a temperature-dependent relationship given in Ref. [19].

Plastic deformation of the metallic frame/interconnect made of Crofer 22-APU was predicted to take place at both room and high temperatures when the Tresca equivalent stress (TES) exceeded the yield strength of the Crofer 22-APU. The G-18 glass ceramic was assumed to behave only in a linear elastic manner at RT but non-linear inelastic behavior was also allowed at operating temperature. In this regard, failure of the glass–ceramic sealant at RT was defined when the maximum principal stress (MPS) exceeded the tensile strength while Tresca criterion was applied at operating temperature. Note that TES is twice the maximum shear stress at a point. Other components such as the PEN, nickel mesh, and mica seal gasket were assumed to deform elastically in solving the thermal stress distribution. Hence, failure of the PEN was defined when the MPS exceeded the ultimate tensile strength of the material. The functions of the nickel mesh are to provide electrical conduction between electrodes and interconnect and to act as a gas channel. The stresses in the nickel mesh were calculated but failure of this part was not considered due to its great flexibility leading to small thermal stresses. Details of the mechanical strength of each given material at room and high temperatures, except the phlogopite mica, were given in [12]. The mica material is brittle at both room and operating temperatures. Hence, failure of the mica gasket was defined when the MPS exceeded the ultimate tensile strength of the material. The tensile strength of the mica sealant parallel to (0 0 1)-plane is about 37 MPa at RT which was determined in house by conducting a tensile test. As described above, a uniform compressive load ranging from 0.06 to 6 MPa was applied during the FEA simulation to assemble the given pSOFC stack. It is expected that such a compressive load would not generate significant out-of-plane stresses in the pSOFC components, compared to the in-plane stresses. Hence, the maximum in-plane principal stress (MIPPS) was used for the PEN, mica gasket, and glass ceramic sealant (at RT) to compare with the corresponding ultimate tensile strength for failure judgment in the following discussion. Although failure may occur at the interface between two connecting components in practical operation, the interfacial fracture strength was not taken into account in this study. Only failure of bulk material was considered. In the analysis procedure, the thermal stress distribution in each SOFC stack component was first determined by the FEA model and then the critical stress values were compared with the corresponding material strength according to the aforementioned criteria.

2.4. Boundary and constrained conditions

The bottom plate of the 3-cell stack, shown in Figs. 1 and 2, was assumed under a plane-support condition such that the entire bottom surface of the bottom plate was constrained in the direction normal to it, i.e. supported over the entire bottom surface by a rigid foundation. On the top plate of the pSOFC stack, a uniformly distributed, compressive load of various magnitudes given in Section 2.2 was applied. In general, stresses caused by self-weight of SOFC components are relatively small compared to thermal stresses such that they were neglected in the simulation. The symmetric plane was constrained in the direction normal to it and the center point was fully constrained to prevent a rigid body motion of the whole stack model. In this model, a "tight-bonding constraint" condition was set between the glass–ceramic seal and the connecting PEN plate and window frame. The interfaces between other connecting pairs of components, including PEN with interconnect, PEN with nickel mesh, nickel mesh with interconnect, mica gasket with PEN-supporting frame, and mica gasket with interconnect,

were all constrained by a "contact constraint" condition in the FEA modeling.

3. Results and discussion

3.1. Effects of applied load in compressive sealing design

In the current study, five different assembly loads (0.06, 0.1, 0.6, 1, and 6 MPa) were applied to investigate the stress distributions in a 3-cell pSOFC stack for use of mica seal gaskets based on the simulation procedures shown in Fig. 4. In order to illustrate the thermal stress distributions in the given pSOFC stack at various stages of an operation cycle, the calculated stress fields for each component in the case with an applied compressive load of 0.6 MPa are presented in details as an example. For the other cases, instead of showing the detailed stress fields in each component, only the critical stress values at various stages are listed in form of tables to compare with the case of 0.6 MPa. Only the greatest MIPPS and maximum Tresca equivalent stress (MTES), hereafter also called the critical stresses, in each component of the entire 3-cell stack model were identified and discussed.

Fig. 5 shows the distributions of the MIPPS in the PENs at the (a) after-assembly, (b) steady-operation, and (c) shutdown stages for an applied compressive load of 0.6 MPa. As shown in Fig. 5, the stress distributions in the PENs at the two RT stages (after-assembly and shutdown) are comparable, but those at the steady-operation stage are quite different from the RT ones. For each stage, the calculated stress field in the PEN of each unit cell in the given 3-cell stack was very close to each other indicating a negligible effect of cell position on the stress distribution. This is because the temperature difference between RT and operating temperature was so large that the thermal stresses dominated the stress distribution in the PEN, compared to the compressive load applied at the top plate. Note that the temperature profiles in the top, middle, and bottom cells for the given pSOFC stack are of little difference, as shown in Fig. 3 [12]. As a result, the stress fields in the top, middle, and bottom PENs were comparable for a given stage. As shown in Fig. 5, the regions having higher MIPPSs in the PENs at each stage are typically located at the edges. Note that these edge areas in the PENs were tightly bonded with the glass–ceramic sealant. In this regard, the CTE mismatch was indeed the major factor to generate the critical thermal stresses in the PEN.

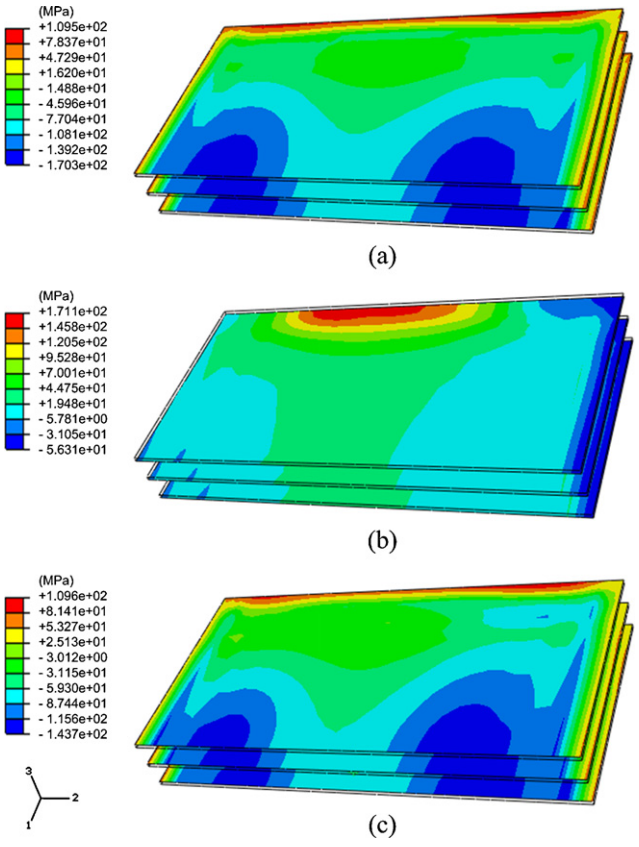

Fig. 5. Distributions of the MIPPS in the PENs at the (a) after-assembly, (b) steady-operation, and (c) shutdown stages for an applied compressive load of 0.6 MPa.

The critical stress in the PENs at the after-assembly stage was about 110 MPa, as shown in Fig. 5(a). Since this critical stress was lower than the corresponding fracture strength of a PEN assembly at RT (187 MPa) [19], no failure of the PENs was predicted to take place after the assembly process. When the given pSOFC stack entered into the steady-operation stage, the critical stress was increased to a value of 171 MPa, as shown in Fig. 5(b). The operating temperature at this critically stressed edge region was around 750 °C and the corresponding fracture strength of the PEN assembly at this temperature was estimated to be 120 MPa. Thus, failure was predicted to take place at certain edges of the PENs under steady-operation. Although failure was predicted in the PEN at a small edge region, the thermal stresses in the inner portion of the PEN, which is the major working area for electrochemical reaction, were lower than the fracture strength. However, this highly critical stress value at the PEN edges might be overestimated due to lack of consideration of friction between adjacent sliding components in the modeling. Further discussion on this issue is given in next section. The stress distribution in Fig. 5(b) shows an asymmetrical pattern, different from that at the after-assembly stage. This is due to an asymmetrical thermal field at the steady-operation stage. The unsymmetrical, non-uniform temperature distribution is mainly due to two reasons: (1) heat generated by electrochemical reactions is most intense near the fuel inlet and (2) airflow is most effective at cooling near the air inlet [12,17]. Note that in the current pSOFC stack model, the fuel inlet is located at the left end in Fig. 2 while the air inlet is located at the right end. Detailed discussion on the temperature patterns at steady-operation for this pSOFC stack design is given elsewhere [12,17]. When the model was re-cooled to RT from the steady-operation stage, the stress distribution at the shutdown stage (Fig. 5(c)) was somewhat like that of the after-assembly stage (Fig. 5(a)) and the critical stresses in both RT stages were comparable.

The PEN-supporting window frames always have the highest stress among the metallic frames/interconnects at all stages. Although the mechanical assembly load was directly applied on the metallic top plate, the critical stresses did not take place at the top plate. This indicates that thermal effects dominated the mechanical loading in generation of stresses in the metallic frames/interconnects. Fig. 6(a) shows the distribution of TES in the window frames at the after-assembly stage. The critical stress, 279 MPa, was located at the inner edge adjacent to the glass–ceramic sealant and exceeded the yield strength of the Crofer 22-APU alloy at RT. Localized plastic deformation was thus predicted to take place in the PEN-supporting frames. Such a high stress was caused by the CTE mismatch among the ceramic PEN, glass–ceramic sealant, and metallic frame. When the model was at the steady-operation stage, the critical stress was reduced to about 71 MPa at the right inner corner (Fig. 6(b)) which was greater than the yield strength of the Crofer 22-APU at the corresponding temperature. Localized plastic deformation was also predicted to take place at this stage in the window frames. When re-cooled to RT, the critical stress was slightly reduced to 251 MPa, compared to the after-assembly stage, but with an increase in the highly stressed area, as shown in Fig. 6(c). Note such an MTES value of 251 MPa was lower than the corresponding yield strength at RT, 268 MPa.

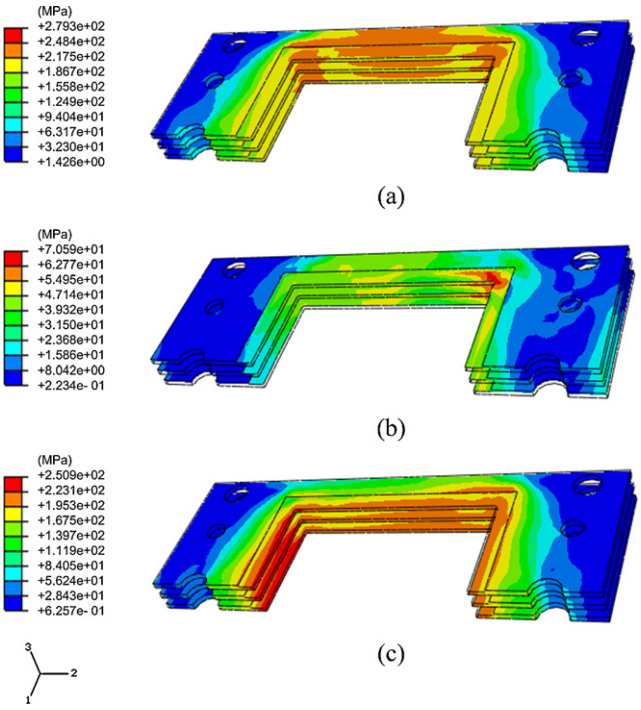

Fig. 6. Distributions of the TES in the PEN-supporting window frames at the (a) after-assembly, (b) steady-operation, and (c) shutdown stages for an applied compressive load of 0.6 MPa.

Fig. 7 shows the distributions of MIPPS in the mica gasket layers at the (a) after-assembly, (b) steady-operation, and (c) shutdown stages for an applied compressive load of 0.6 MPa. Note that only the layers with the greatest MIPPS at each stage are presented in Fig. 7. As shown in Fig. 7(a) and (c), the stress distributions in the mica sealants at the two RT stages were similar and had critical stresses of 26 and 30 MPa, respectively, which were lower than its tensile strength 37 MPa at RT. The critical stress at the steady-operation stage (14 MPa) was smaller and the distribution was more uniform, as shown in Fig. 7(b).

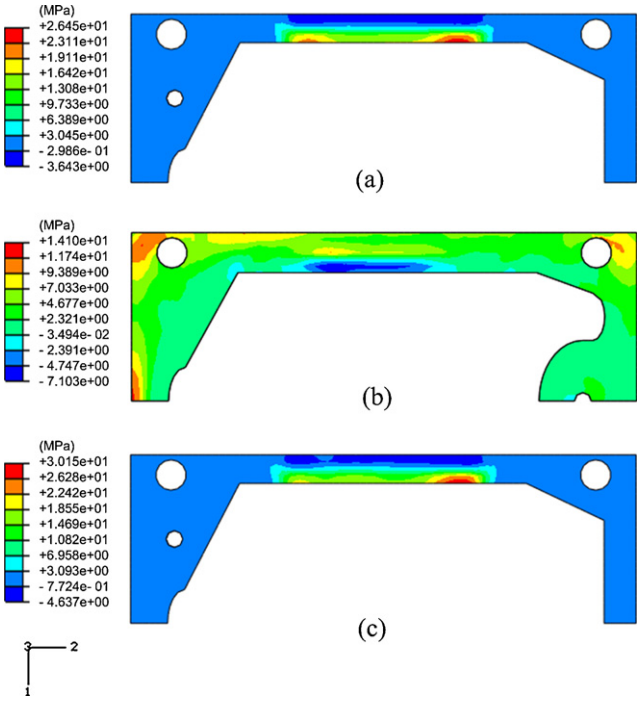

Fig. 7. Distributions of the MIPPS in the most severely stressed mica layer at the (a) after-assembly, (b) steady-operation, and (c) shutdown stages for an applied load of 0.6 MPa.

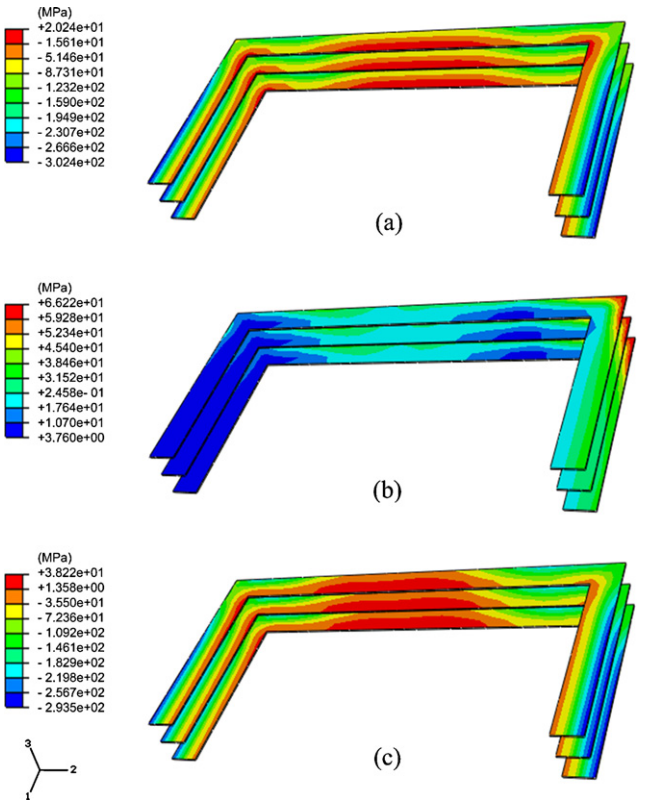

Fig. 8. Stress distributions in the peripheral glass–ceramic sealants at the (a) after-assembly (MIPPS), (b) steady-operation (TES), and (c) shutdown (MIPPS) stages for an applied load of 0.6 MPa.

Fig. 8 shows the stress distributions in the glass–ceramic sealants at the (a) after-assembly, (b) steady-operation, and (c) shutdown stages for an applied compressive load of 0.6 MPa. The greatest MIPPS at the after-assembly stage was about 20 MPa which occurred at the inner edges and corners adjacent to the PENs, as shown in Fig. 8(a). When the stack model adopted the temperature distribution at the steady-operation stage, the MTES in the glass–ceramic sealant was about 66 MPa at the right outer corner, as shown in Fig. 8(b). An MTES value of 66 MPa is equivalent to a maximum shear stress of 33 MPa. As described in an early study [12], such a maximum shear stress was presumably greater than the corresponding shear strength of G-18 such that shear fracture of the glass–ceramic sealant at the right outer corner regions was likely to occur at steady-operation. However, further experimental verification and detailed viscoelastic or viscoplastic analysis for this issue is needed, as the glass–ceramic sealant would become viscous to relax the stress to certain extents [12]. At the shutdown stage, the stress distribution pattern is very similar to that at the after-assembly stage but with a greater MIPPS value of 38 MPa, as shown in Fig. 8(c). Again, such an increase in the greatest MIPPS at RT may result from the plastic deformation of the metallic frame at the steady-operation stage. This critical stress of 38 MPa is lower than its flexural strength at RT, 48 MPa [21].

Table 2 summarizes the critical stresses, described above, in various components at all stages for a mechanically applied compressive load of 0.6 MPa. Generally speaking, the critical stresses in the PENs, glass–ceramic sealants, and PEN-supporting window frames were located at their co-sintered boundaries because of thermal expansion mismatch. At the steady-operation stage, all

Table 2
Critical stresses for an applied assembly load of 0.6 MPa.

Stage	PEN	Nickel mesh	Mica	IC[a]/frame	Glass–ceramic sealant	
	MIPPS (MPa)	MTES (MPa)	MIPPS (MPa)	MTES (MPa)	MIPPS (MPa)	MTES (MPa)
After-assembly	109.5	13.83	26.45	279.3	20.24	–
Steady-operation	171.1	9.400	14.10	70.59	–	66.22
Shutdown	109.6	14.12	30.15	250.9	38.22	–

[a]IC: interconnect.

Table 3
Critical stresses for an applied assembly load of 0.06 MPa.

Stage	PEN	Nickel mesh	Mica	IC/frame	Glass–ceramic sealant	
	MIPPS (MPa)	MTES (MPa)	MIPPS (MPa)	MTES (MPa)	MIPPS (MPa)	MTES (MPa)
After-assembly	119.4	14.46	24.54	283.3	8.516	–
Steady-operation	171.6	9.385	13.88	70.52	–	64.65
Shutdown	119.8	14.57	24.91	253.5	27.82	–

Table 4
Critical stresses for an applied assembly load of 0.1 MPa.

Stage	PEN	Nickel mesh	Mica	IC/frame	Glass–ceramic sealant	
	MIPPS (MPa)	MTES (MPa)	MIPPS (MPa)	MTES (MPa)	MIPPS (MPa)	MTES (MPa)
After-assembly	118.0	13.82	23.98	282.4	8.901	–
Steady-operation	171.4	9.511	13.86	70.80	–	66.73
Shutdown	118.2	14.06	25.20	252.8	26.12	–

components show an asymmetric stress distribution due to the asymmetric thermal field. The stress distributions in the PEN and glass–ceramic sealant at the shutdown stage were influenced by the plastic deformation of the metallic window frames and the associated residual stresses. The corresponding stress distributions in the PENs, glass–ceramic sealants, window frames, and nickel meshes of the top, middle, and bottom cells were almost the same which is consistent with a previous study [12]. This means that the thermal stress distribution in a pSOFC stack with an applied compressive load of 0.6 MPa does not vary significantly with the cell position.

Tables 2–6 list the critical stresses in various components at all stages for each applied assembly load. As the applied compressive load on the stack was increased from 0.06 to 0.1 MPa, the critical stresses for each component had no obvious change (Tables 3 and 4). For a further increase of the applied load to a level of 0.6 MPa, the critical stresses in the glass–ceramic sealant at the two RT stages were increased (Table 2). The critical stress in the mica layer for a 0.6 MPa compressive load was also increased as a result of the increasing contact pressure. Similar trends were also observed for a greater increase of the applied compressive load to 1 and 6 MPa in both the glass–ceramic and mica sealants (Tables 5 and 6). However, the critical stress in the PENs tended to slightly decrease with an increase in the applied load to a level equal to and larger than 0.6 MPa. This phenomenon was associated with existence of a bending deformation in the PEN and its supporting window frame under a smaller level of applied load. Increasing the applied compressive load to a level equal to or greater than 0.6 MPa could eliminate the bending deformation in the PEN-frame assembly plate. The critical stress in the mica layer was increased with increasing applied load due to a greater direct-contact pressure for a lower gas leakage rate. By assuming the strength of the mica at the operating temperature is equal to that at RT (37 MPa), the mica was predicted to work safely at the steady-operation stage for a compressive load up to 6 MPa. However, the critical stress in the mica at both RT stages for a 6 MPa compressive load was very close to its tensile strength. In addition, the critical stress at the shutdown stage in the glass–ceramic sealant for a 6 MPa compressive load was 51 MPa which exceeded its flexural strength at RT, 48 MPa [21]. In this regard, a 0.6 MPa compressive load seems to be an optimal assembly load that can both eliminate the bending deformation in the PEN-frame assembly plate and maintain an acceptable critical stress in the glass–ceramic sealant.

Table 5
Critical stresses for an applied assembly load of 1 MPa.

Stage	PEN	Nickel mesh	Mica	IC/frame	Glass–ceramic sealant	
	MIPPS (MPa)	MTES (MPa)	MIPPS (MPa)	MTES (MPa)	MIPPS (MPa)	MTES (MPa)
After-assembly	107.2	13.97	27.84	276.8	22.44	–
Steady-operation	168.1	9.375	14.49	69.65	–	66.09
Shutdown	107.1	14.03	30.59	249.8	40.80	–

Table 6
Critical stresses for an applied assembly load of 6 MPa.

Stage	PEN	Nickel mesh	Mica	IC/frame	Glass–ceramic sealant	
	MIPPS (MPa)	MTES (MPa)	MIPPS (MPa)	MTES (MPa)	MIPPS (MPa)	MTES (MPa)
After-assembly	108.4	13.86	34.20	268.6	37.29	–
Steady-operation	169.2	9.434	17.88	70.40	–	66.22
Shutdown	106.6	14.12	36.19	243.3	51.65	–

Table 7
Critical stresses for mechanical-load-only conditions without thermal effects.

Applied load (MPa)	PEN MIPPS (MPa)	Nickel mesh MTES (MPa)	Mica MIPPS (MPa)	IC/frame MTES (MPa)	Glass–ceramic sealant MIPPS (MPa)
0.06	0.092	0.006	0.170	0.398	0.087
0.1	0.154	0.010	0.283	0.663	0.146
0.6	0.923	0.061	1.698	3.982	0.873
1	1.538	0.102	2.829	6.637	1.456
6	9.255	0.605	16.83	39.76	8.741

Table 8
Critical stresses in the case using only glass–ceramic sealants [12].

Stage	PEN	Nickel mesh	IC/frame	Glass–ceramic sealant	
	MIPPS (MPa)	MTES (MPa)	MIPPS (MPa)	MTES (MPa)	MIPPS (MPa)
After-assembly	169.4	16.25	321.3	13.77	–
Steady-operation	69.57	9.859	83.13	–	65.59
Shutdown	175.1	18.85	320.6	38.26	–

In order to quantitatively evaluate the effect of the applied load on the stress distribution, a mechanical-load-only simulation was also conducted. Table 7 shows the critical stresses under five different compressive loads without consideration of thermal effects. The critical stress for a given component increased linearly with the applied load implying the components were all under a linear elastic condition and the boundary conditions were not changed. Since all the stress contours were similar, only the stress distribution for a 0.6 MPa compressive load was presented. Fig. 9 shows the stress distributions in the PENs, glass–ceramic sealants, and mica layer under a compressive load of 0.6 MPa with no temperature variation involved. By comparing the stress distributions between the models with and without thermal field data involved, some conclusions can be made. The critical stresses in the PENs and metallic

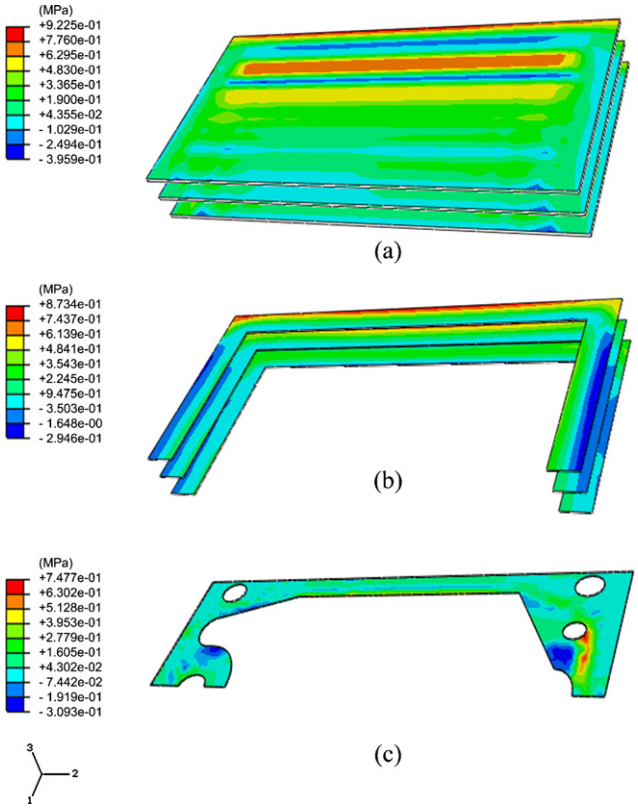

Fig. 9. Distributions of the MIPPS in the (a) PENs, (b) glass–ceramic sealants, and (c) mica layer for a 0.6 MPa compressive load without consideration of the temperature variation.

frames/interconnects in an operation cycle were mainly governed by the temperature changes and gradients. Similarly, for the mica layer, although its critical stress increased with applied compressive load, the critical stress with thermal field was significantly larger than that without thermal effects. The stresses generated in the glass–ceramic sealant during an operation cycle were also controlled by the thermal effects. Apparently, thermal expansion mismatch played a predominant role over the applied assembly load in determining the stress level and distribution for a pSOFC stack during an operation cycle.

3.2. Effects of sealing design

In an early study [12], a rigid-bonding type of seal, G-18 glass ceramic, was used as the only sealing material to join the components such as the PENs with the supporting window frames and the interconnects with the frames. The critical stresses in each component for such a rigid sealing design at a plane-supported condition are listed in Table 8 [12] for comparison with the results of the present work. In the current study, the sealant at the interface between the PEN-supporting window frame and interconnect was replaced by a compressive mica seal gasket. The critical stresses in the current compressive sealing design and the pervious rigid sealing design are made a comparison through Tables 2 and 8. The critical stresses in the metallic interconnect and window frame at all stages tended to decrease when the glass–ceramic sealant was replaced by the mica gasket. This could be attributed to that the compliant mica sealant allowed a slide between the adjacent window frame and interconnect. The critical stresses in both the nickel mesh and glass–ceramic sealant did not show significant difference between these two sealing designs. However, the critical stresses in the PENs for the two different sealing designs showed an opposite trend at operating and room temperatures. When the glass–ceramic sealant between the adjacent metal layers was replaced by a mica gasket, the critical stress in the PEN was reduced from about 170 to 110 MPa at RT and increased from about 70 to 171 MPa at operating temperature. This comparison indicates that the stress-strain behavior of a pSOFC stack was significantly influenced by the contact condition between the sealant and adjacent metallic window frame and interconnect. Changing the contact behavior between the sealant and adjacent metal layers also changed the bending behavior of the PEN-frame assembly plate and associated stress level and distribution. For example, the calculated, maximum bending deflection for the center point of the PEN-frame assembly plate at the steady-operation stage was 6.92×10^{-4} mm in the compressive sealing design under an applied assembly load of 0.6 MPa while the counterpart in the rigid sealing design was 2.66×10^{-1} mm.

Table 9
Critical stresses for an applied assembly load of 0.6 MPa with a uniform operating temperature of 800 °C.

Stage	PEN	Nickel mesh	Mica	IC/frame	Glass–ceramic sealant	
	MIPPS (MPa)	MTES (MPa)	MIPPS (MPa)	MTES (MPa)	MIPPS (MPa)	MTES (MPa)
After-assembly	109.5	13.83	26.45	279.3	20.24	–
Steady-operation	73.44	0.360	7.070	43.88	–	20.13
Shutdown	103.4	13.83	27.71	277.3	20.04	–

In this regard, a compliant mica sealant could ease the stress in the bonded areas of the connecting metallic layers and change the deformation in the PEN-frame assembly plate.

In order to further understand the different stress distributions in the PENs between the two sealing designs, some additional simulations were conducted. In an additional simulation, a uniform temperature distribution of 800 °C, instead of the temperature distribution given in Fig. 3, was assumed at the steady-operation stage for the compressive sealing case under an applied compressive load of 0.6 MPa. Table 9 lists the critical stresses calculated by such a simulation. The critical stress in the PEN at the steady-operation stage was significantly reduced to 73 MPa which was much lower than the corresponding value of 171 MPa given in Table 2. Fig. 10 shows the stress distributions in the PENs at the steady-operation stage with a uniform temperature field of 800 °C under an applied load of 0.6 MPa. By comparing Figs. 10 and 5(b), it can be concluded that the greater critical stress in the PEN at the steady-operation stage for the case presented in Table 2 and Fig. 5(b) was mainly due to a temperature gradient effect. Not only the critical stress in the PEN but also that in the glass–ceramic sealant at the steady-operation stage was substantially reduced by such a uniform distribution of operating temperature. Hence, designing a pSOFC stack with more uniform electrochemical reaction activities and less temperature gradients could lower the critical stress level and improve the structural integrity.

Moreover, the highly critical stresses in the PENs under steady-operation for the compressive sealing design might be overestimated. The friction between the mica gasket and adjacent metallic layers was neglected in the simulations described above. In order to estimate the friction effect, a static friction coefficient of 0.3 was introduced at the interfaces between the mica gaskets and adjacent metallic layers in another additional simulation. The stress distributions at the steady-operation stage in the PENs for a stack with friction involved under a compressive load of 0.6 MPa were calculated and shown in Fig. 11. As shown in Fig. 11, the critical stress in the PEN at the steady-operation stage was reduced from 171 to 150 MPa at a similar location to that presented in Fig. 5(b). Apparently, friction between the mica gasket layers and adjacent metallic window frames and interconnects also influenced the critical stress level of the PEN to a certain extent in a pSOFC stack.

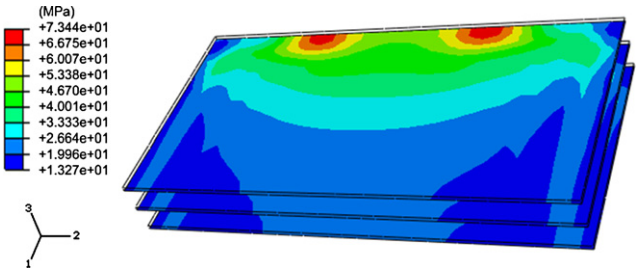

Fig. 10. Distributions of the MIPPS in the PENs at the steady-operation stage for an applied load of 0.6 MPa with a uniform temperature distribution of 800 °C.

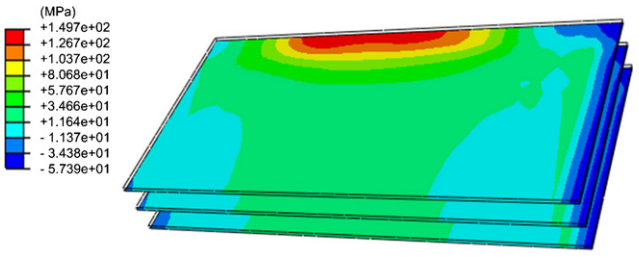

Fig. 11. Distributions of the MIPPS in the PENs at the steady-operation stage for an applied load of 0.6 MPa with consideration of friction effects between the mica gaskets and connecting metallic layers.

4. Conclusions

(1) For a 3-cell pSOFC stack using compliant mica gaskets to seal the interfaces between the metallic PEN-supporting window frames and interconnects, increasing the applied assembly load from 0.06 to 0.6 MPa could eliminate the bending deformation in the PEN and its supporting frame. For a further increase of the applied compressive load to 1 and 6 MPa, the critical stresses in the glass–ceramic and mica sealants at RT tended to increase to a potential failure level. In this regard, a 0.6 MPa compressive assembly load is considered an optimal assembly load that can both eliminate the bending deformation in the PEN-frame assembly plate and maintain acceptable critical stresses in the glass–ceramic and mica sealants.

(2) For the given 3-cell pSOFC stack using compliant mica-based seals under a compressive assembly load of 0.6 MPa, the calculated thermal stresses in the PENs, metallic interconnects and frames, mica gaskets, and glass–ceramic sealants at RT (after-assembly and shutdown stages) were lower than the corresponding fracture strength while localized plastic deformation in the PEN-supporting frames was predicted. At operating temperature, the critical stresses in the PENs and glass–ceramic sealants at certain edge areas were greater than the corresponding fracture strength and localized plastic deformation was also predicted for the PEN-supporting frames. However, by adding a friction effect on the interface between the mica gaskets and connecting metallic layers in the modeling, the critical stresses in the PENs were favorably reduced. The highly stressed regions of the PEN, glass–ceramic sealant, and PEN-supporting frame were located at the co-sintered boundaries as a result of thermal expansion mismatch.

(3) For the given 3-cell pSOFC stack using compliant mica-based seals, stress distributions in the PEN, PEN-supporting frame, interconnect, and nickel mesh were mainly governed by the CTE mismatch under a large temperature difference and thermal gradients and barely influenced by the applied compressive load.

(4) Replacement of the glass–ceramic sealant by a mica seal gasket in joining the connecting metallic PEN-supporting frame and interconnect would cause a dramatic stress change in the PEN. The critical stress in the PEN was favorably decreased at RT but significantly increased at the operating temperature due to such a change in sealing design. This could be attributed to the effects of the constrained conditions of interfacial bonding on the deformation of the PEN-frame assembly plate.

Acknowledgements

This work was supported by the Institute of Nuclear Energy Research and National Science Council (Taiwan) under Contract Nos. NSC 96-NU-7-008-002 and 97-2001-INER-037.

References

[1] J.W. Fergus, J. Power Sources 147 (2005) 46–57.
[2] S.P. Simner, J.W. Stevenson, J. Power Sources 102 (2001) 310–316.
[3] H. Yakabe, Y. Baba, T. Sakurai, M. Satoh, I. Hirosawa, Y. Yoda, J. Power Sources 131 (2004) 278–284.
[4] H. Yakabe, Y. Baba, T. Sakurai, Y. Yoshitaka, J. Power Sources 135 (2004) 9–16.
[5] W. Fischer, J. Malzbender, G. Blass, R.W. Steinbrech, J. Power Sources 150 (2005) 73–77.
[6] C.S. Montross, H. Yokokawa, M. Dokiya, Br. Ceram. Trans. 101 (2002) 85–93.
[7] T. Zhang, Q. Zhu, W.L. Huang, Z. Xie, X. Xin, J. Power Sources 182 (2008) 540–545.
[8] H. Yakabe, T. Ogiwara, M. Hishinuma, I. Yasuda, J. Power Sources 102 (2001) 144–154.
[9] A. Selimovic, M. Kemm, T. Torisson, M. Assadi, J. Power Sources 145 (2005) 463–469.
[10] J. Laurencin, G. Delette, F. Lefebvre-Joud, M. Dupeux, J. Euro. Ceram. Soc. 28 (2008) 1857–1869.
[11] L.-K. Chiang, H.-C. Liu, Y.-H. Shiu, C.-H. Lee, R.-Y. Lee, Renew. Energ. 33 (2008) 2580–2588.
[12] C.-K. Lin, T.-T. Chen, Y.-P. Chyou, L.-K. Chiang, J. Power Sources 164 (2007) 238–251.
[13] K.S. Weil, B.J. Koeppel, Int. J. Hydrogen Energ. 33 (2008) 3976–3990.
[14] K.S. Weil, B.J. Koeppel, J. Power Sources 180 (2008) 343–353.
[15] ABAQUS Analysis User's Manual, Volume IV: Elements, Version 6.5, ABAQUS, Inc., Providence, RI, USA, 2004, pp. 15.6.1-1-15.6.10-5.
[16] S. Le, K. Sun, N. Zhang, Y. Shao, M. An, Q. Fu, X. Zhu, J. Power Sources 168 (2007) 447–452.
[17] Y.P. Chyou, T.D. Chung, J.S. Chen, R.F. Shie, J. Power Sources 139 (2005) 126–140.
[18] S. Habelitz, G. Carl, C. Rüssel, S. Thiel, U. Gerth, J.-D. Schnapp, A. Jordanov, H. Knake, J. Non-Cryst. Solids 220 (1997) 291–298.
[19] K.S. Weil, J.E. Deibler, J.S. Hardy, D.S. Kim, G.-G. Xia, L.A. Chick, C.A. Coyle, J. Mater. Eng. Perform. 13 (2004) 316–326.
[20] Y.-S. Chou, J.W. Stevenson, J. Power Sources 124 (2003) 473–478.
[21] N.P. Bansal, J.B. Hurst, S.R. Choi, J. Am. Ceram. Soc. 89 (2006) 388–390.